

Article

Influence of Fiber Dimensions on Bridging Performance of Polyvinyl Alcohol Fiber-Reinforced Cementitious Composite (PVA-FRCC)

Helen Negash Shiferaw ¹, Selamawit Fthanegest Abrha ¹, Toshiyuki Kanakubo ^{2,*},
Madappa V. R. Sivasubramanian ³ and Shamsher Bahadur Singh ⁴

- ¹ Degree Program in Engineering Mechanics and Energy, University of Tsukuba, Tsukuba 305-8573, Japan; s2365064@u.tsukuba.ac.jp (H.N.S.); s2220902@u.tsukuba.ac.jp (S.F.A.)
- ² Division of Engineering Mechanics and Energy, University of Tsukuba, Tsukuba 305-8573, Japan
- ³ Department of Civil Engineering, National Institute of Technology Puducherry, Puducherry 609 609, India; madappa@nitpy.ac.in
- ⁴ Department of Civil Engineering, Birla Institute of Technology and Science, Pilani 333 031, India; sbsingh@pilani.bits-pilani.ac.in
- * Correspondence: kanakubo@kz.tsukuba.ac.jp

Abstract: This study investigates the influence of fiber dimensions on the bridging performance of polyvinyl alcohol fiber-reinforced cementitious composite (PVA-FRCC) through an experimental and analytical program. Bending tests, bridging law calculations, and section analysis are conducted. Bending tests of notched specimens of PVA-FRCC with six different PVA fiber dimensions are performed to determine the load–deflection (LPD) and bending moment–crack mouth opening displacement (CMOD) relationships. The fiber volume fraction for all PVA-FRCCs is set to 2%. It is found that the load capacity of PVA-FRCC with a 27 μm diameter fiber is much higher than that of the other fibers, and the load capacity decreases as the fiber diameter increases. The study proposes parameters for the characteristic points of the tri-linear model for the single-fiber pullout model as functions of diameter, bond fracture energy, elastic modulus, cross-sectional area, and perimeter of the fiber. These findings provide valuable insights into the behavior of PVA-FRCC under different fiber dimensions. Bridging law calculations are conducted to obtain tensile stress–crack width relationships using the developed single-fiber pullout models. The Popovics model for the complete tensile stress–crack width relationship is adopted to obtain a better fit with the bridging law calculation, and then section analysis is conducted. The bridging law calculation results show that the maximum tensile stress decreases as the fiber diameter increases. It is also determined that most of the smaller-diameter fibers ruptured, whereas the larger fiber diameters pulled out from the matrix. The section analysis results show good agreement with the maximum bending moments obtained from the bending test.

Keywords: PVA-FRCC; fiber dimension; fiber diameter; bending test; single-fiber pullout model; bridging law calculation; section analysis



Citation: Shiferaw, H.N.; Abrha, S.F.; Kanakubo, T.; Sivasubramanian, M.V.R.; Singh, S.B. Influence of Fiber Dimensions on Bridging Performance of Polyvinyl Alcohol Fiber-Reinforced Cementitious Composite (PVA-FRCC). *Fibers* **2024**, *12*, 70. <https://doi.org/10.3390/fib12080070>

Academic Editor: Damien Soulat

Received: 1 August 2024

Revised: 16 August 2024

Accepted: 20 August 2024

Published: 22 August 2024



Copyright: © 2024 by the authors. Licensee MDPI, Basel, Switzerland. This article is an open access article distributed under the terms and conditions of the Creative Commons Attribution (CC BY) license (<https://creativecommons.org/licenses/by/4.0/>).

1. Introduction

Compared to other building materials like steel, wood, composite systems, etc., concrete is more durable and offers a higher strength-to-cost ratio, but it still has a few drawbacks. Brittle behavior and decreased tensile strength are the primary drawbacks of employing concrete in structural applications [1–6]. During the 1970s, it was recognized and observed that adding randomly distributed discrete fibers to the cementitious matrix to create a fiber-reinforced cementitious composite (FRCC) might improve the tensile strength, flexural strength, and ductility of the material [2,3,7–9]. Various fiber types are available in a range of diameters and forms. Steel fiber (SF), carbon fiber (CF), synthetic polymer fibers,

such as polyethylene (PE), polyvinyl alcohol (PVA), polypropylene (PP), aramid fiber, and natural fibers, are the main types of fiber used in FRCC [10–14].

With the expectation of exhibiting high fracture toughness, deformability, and small crack openings, the characteristics of FRCCs can provide increased performance for the structural behavior of concrete constructions and great durability against environmental attacks [15–17].

Polymeric fibers are advantageous in construction due to their superior chemical resistance to steel fibers, which are commonly used in structural elements. Although steel fibers offer excellent mechanical properties and durability, they have drawbacks such as increased weight and cost. The corrosion of steel fibers in aggressive environments can compromise their crack-bridging ability and the appearance of concrete structures, leading to reduced strength and aesthetic appeal. This corrosion can result in concrete spalling and decreased fiber cross-sectional area, significantly impacting structural durability. In contrast, polymer fibers exhibit high resistance to corrosion, alkaline reactions, acidic water, salt, chlorine, chemicals, and microorganisms. Therefore, incorporating polymeric fibers as reinforcement in cementitious materials enhances mechanical properties and durability and reduces structural weight and construction costs [18].

The development of high-strength polymeric fibers, such as PP, PE, and PVA fibers, has coincided with studies on high-performance fiber-reinforced cement composite (HPFRCC) including strain-hardening cement composite (SHCC) and engineered cementitious composite (ECC) since the 1980s. Under tensile studies, these HPFRCCs display repeated cracking and pseudo-strain-hardening behavior. These have been applied in real applications, like earthquake barriers, tunnel linings, decks, and slabs [13,19–22].

FRCC's performances can be identified by measurable characteristics associated with the fiber (elastic modulus, strength, bundle sizes, length, diameter, shape, etc.), the cementitious matrix (strength, porosity, flaw density, fracture property, etc.), and the interface. The selection of composite materials, including volume fraction, fiber types, additives, aggregates, cement type, and processing technique, all affect these characteristics [7,23–28]. One of the most significant fundamental characteristics controlling the response of FRCCs is crack bridging by the fiber. Moreover, it has been shown that crack bridging even regulates structural response [29–32]. Building particular bridging rules for the intended FRCC is required because the pullout behavior varies greatly based on the fiber type and matrix [13].

Various factors, including fibers' type and volume fraction, fiber–matrix bond strength, curing conditions, and loading rate, influence the flexural behavior of fiber-reinforced cementitious composites. Proper selection and orientation of fibers can significantly improve the composite's resistance to bending and enhance its overall performance. The influence of fibers on composites' pre-cracking behavior and initial crack strength is minimal. Still, their characteristics play a significant role in determining the post-cracking behavior of the material. Fiber properties dictate whether the composite displays deflection-hardening, where fibers continue supporting and resisting crack propagation, or deflection-softening behavior, where the material weakens and loses load-carrying capacity as cracks propagate. In essence, fiber characteristics are critical in shaping the post-cracking response of composites, delineating between deflection-hardening and deflection-softening types based on their ability to sustain load and deformation after cracking [24,33].

PVA fiber is one of the most common and extensively researched fibers in the field of improving ductility, reducing the rate at which cracks propagate, and bridging capability in FRCC structures. They offer various benefits, such as improved cracking performance, higher tensile and flexural strength, strain-hardening properties, and enhanced mechanical characteristics. Despite having a lower tensile strain capacity than PE fibers, the strong bond between PVA fibers and cementitious materials increases composite strength and energy absorption capacity. PVA fibers are a cost-effective alternative to PE fibers and are becoming more popular for specific applications. Proper dispersion of PVA fibers in the matrix is essential for achieving optimal mechanical properties, with even small amounts significantly boosting tensile and flexural strengths. The bridging effect of PVA fibers leads

to strain-hardening and the formation of multiple cracks in PVA-FRCC, further improving its performance [4,15,18,34–38].

The main objective of this research is to study the influence of fiber dimensions on the bridging performance of PVA-FRCC. Although the bridging effect has been investigated using PVA fibers of various dimensions, few studies have conducted a unified investigation of the differences in fiber dimensions. In this study, an experimental program of bending test using notched specimens and section analysis is performed with the main experimental parameter as fiber dimensions (diameter and length). Six types of PVA fiber dimensions are considered. Kanakubo et al. developed a single-fiber pullout model for PVA fiber with a diameter of 100 μm and 12 mm in length [39]. The single-fiber pullout model for the other fiber dimensions was developed based on this developed model. The parameters that give the characteristic points of the tri-linear model for the single-fiber pullout model are proposed as functions of diameter, bond fracture energy, elastic modulus, cross-sectional area, and perimeter of the fiber. The tensile stress–crack width relationship is developed using a bridging law calculation, that uses the single fiber pullout model as a main input. Popovics model of complete tensile stress–crack width relationship is adopted to obtain a better fit with the bridging law calculation. Then, a section analysis is conducted to check the adaptability of the developed model to the experimental program. The capability to evaluate the bridging effect in a unified manner for fibers of various dimensions will enable the selection of fibers with appropriate dimensions in material design. This unified evaluation approach will enhance the efficiency and effectiveness of material design by allowing the selection of fibers that optimize the bridging effect and improve overall material performance.

2. Experimental Program

2.1. Used Materials

The fiber type used in this study is PVA, provided by Kuraray Co. Ltd., Tokyo, Japan. As shown in Figure 1, this study targets six different PVA fiber dimensions. These fibers are selected based on their availability during the study. The manufacturer regularly produces RMS702 \times 6, REC15 \times 12, RECS100L \times 12, RFS400 \times 18, and RF4000 \times 30, and RF350 \times 12 is made at customer request. The mechanical properties and specimen IDs are listed in Table 1. The specimen ID is a combination of fiber type, fiber diameter, and fiber length. The fiber volume fraction of FRCC used to make the specimens is set to 2% for all the fibers. From previous research, for RCES100L \times 12, which will later be used as a reference fiber, a 2% fiber volume fraction was used to obtain an excellent workable PVA-FRCC mix with good bridging performance [39]. The main objective of this research is to study the influence of fiber dimensions, so the fiber volume fraction is kept constant.

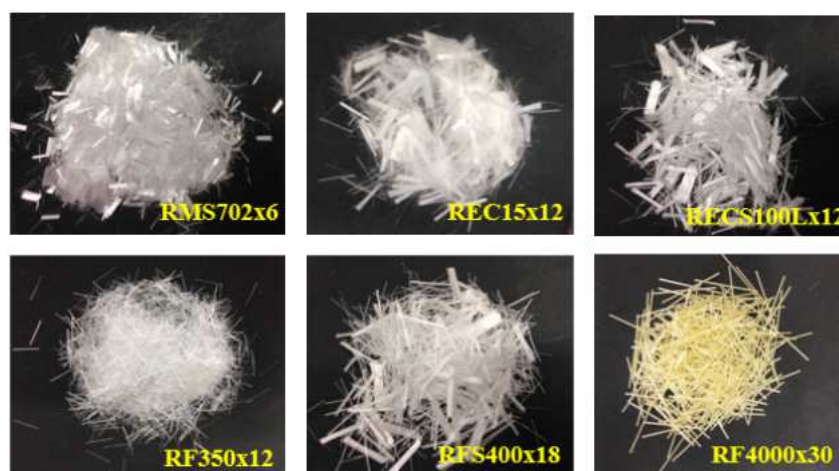


Figure 1. PVA fibers used in this study.

Table 1. Mechanical properties of PVA fiber.

ID	Type	Diameter (μm)	Length (mm)	Tensile Strength (MPa)	Elastic Modulus (GPa)
PVA027-06	RMS702 \times 6	27	6	1800	46
PVA040-12	REC15 \times 12	40	12	1560	41
PVA100-12	RECS100L \times 12	100	12	1200	28
PVA200-12	RF350 \times 12	200	12	910	30
PVA200-18	RFS400 \times 18	200	18	975	27
PVA660-30	RF4000 \times 30	660	30	900	23

Note: The dimensions and mechanical properties are nominal values the manufacturer provides.

The specimens were fabricated using high early-strength Portland cement, with a 56% water–cement ratio. Table 2 shows the mixture proportion adopted for this study.

Table 2. Mixture proportion.

Fiber Volume Fraction	W/C	FA/B	Unit Weight (kg/m^3)			
			Water	Cement	Fly Ash	Sand
2%	0.56	0.3	380	678	291	484

Cement: High early-strength Portland cement
Fly ash: Type II of Japanese Industrial Standard (JIS A 6201 [40])
Sand: Size under 0.2 mm
Super plasticizer: Binder \times 0.6%

The mixing procedure was adopted to ensure easy mixing and obtain a workable mixture. The mixing was performed using a mixture machine with a 60 L capacity. For each specimen, a 30-L mixture was prepared. The dry powder of cement, sand, and fly ash was first mixed for 1 min. Then 95% of the water with superplasticizer was added and mixed for a total of 3 min. The flowability of the mortar was checked by the flowtime using a funnel. The measured flowtime was 20 s on average for all specimens. A 45 g thickener was mixed with the remaining 5% water, then added to the mortar and mixed for 2 min. The flowtime was 45 s on average for all specimens in the second flowability test. To ensure uniform fiber dispersion, the fibers were added to the mortar in two stages, with 50% at each stage, and mixed for 30 s in each stage. After checking the fiber dispersion by the palpation, the mixed FRCC was powered to the prepared molds.

Three ϕ 100 mm by 200 mm cylindrical test pieces are prepared for each specimen ID for the compression test. The specimen ID “N” is given for specimens without fiber. After sealed curing for 7 days, the specimens are left to cure at room temperature. The testing age is 30 days. A 500 kN universal testing machine is used to measure compressive characteristics. The average results of the compression test are shown in Table 3.

Table 3. Compression test result.

Specimen ID	Compressive Strength (MPa)	Elastic Modulus (GPa)
N	45.7	17.2
PVA027-06	49.0	16.1
PVA040-12	37.2	13.2
PVA100-12	47.7	17.0
PVA200-12	45.0	15.8
PVA200-18	43.3	16.3
PVA660-30	47.4	16.4

2.2. Bending Test of Notched Specimens

2.2.1. Specimens

A notched beam with a dimension of 100 \times 100 \times 400 mm with a notch size of 30 mm in depth and 5 mm in width as shown in Figure 2 prepared. Five specimens are prepared for each specimen ID.

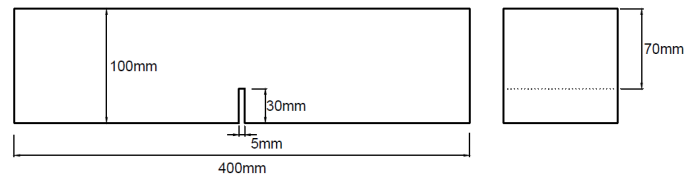


Figure 2. Specimen dimension for bending test.

2.2.2. Loading and Measurements

A three-point bending test is conducted according to ISO 19044 [41] using a 500 kN universal testing machine to investigate the load-displacement characteristics of PVA-FRCC. A linear variable displacement transducer (LVDT) and two Pi-type displacement transducers are used to measure the load point deflection (LPD) and crack mouth opening displacement (CMOD). The CMOD is obtained by converting the axial deformation measured by Pi-type displacement transducers under the assumption that a plain section remains plain. The loading and measurement setup are shown in Figure 3.

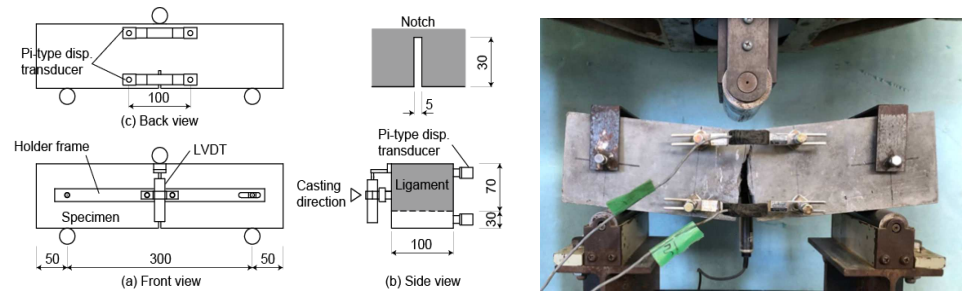


Figure 3. Setup of loading and measurement.

2.2.3. Failure Patterns

Distinct crack patterns based on the presence and characteristics of fibers within the specimen are observed during loading. In the specimen without fiber (N), a single crack emerges and extends directly from the notch to the point of loading. This crack propagation path indicates a clear and linear failure progression within the material. Specimens with smaller fibers generate numerous small and fine cracks at first. Then, as the load increases, a single large crack is generated once the fibers are either ruptured or pulled out. This sequential progression from fine cracks to a major crack highlights the role of smaller-diameter fibers in influencing the specimen’s crack initiation and propagation behavior. Specimens with larger-diameter fibers exhibit a different crack formation pattern. The presence of these larger fibers leads to the generation of one or two major cracks, forming distinct and prominent cracks that open. Figure 4 shows some examples of crack patterns in the specimens.

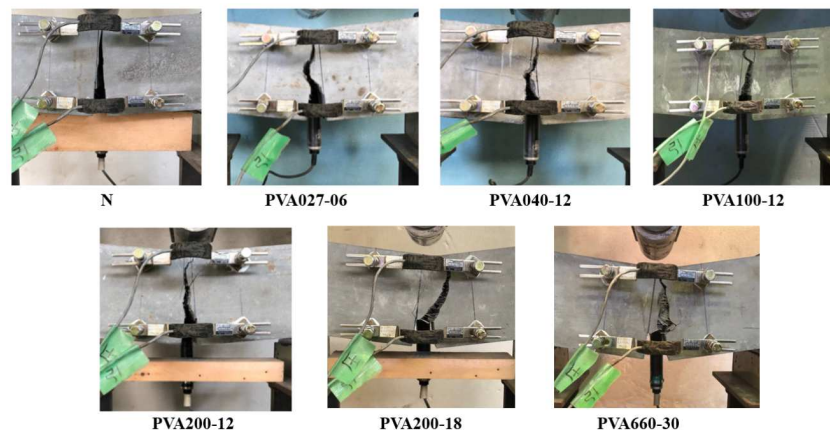


Figure 4. Examples of crack patterns of specimens in bending test.

Figure 5 shows examples of fractured surfaces. The fibers are evenly distributed over the broken surface, as shown in the figure. Most of the fibers in specimens PVA027-06 and PVA040-12 are ruptured, and most of the fibers in specimens PVA200-12, PVA200-18, and PVA660-30 are pulled out.

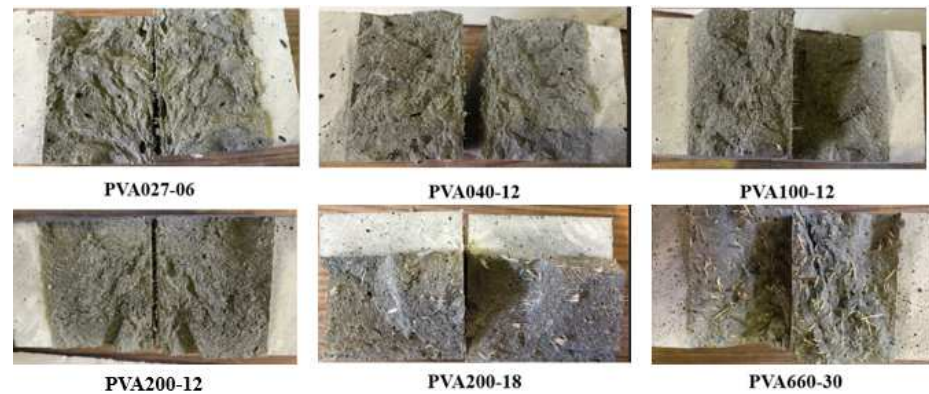


Figure 5. Examples of fractured surface.

2.2.4. Load–Deflection Relationship

The load–deflection relationship obtained from the bending test is shown in Figure 6. One test result of PVA200-18 is discarded because there was an error on the LVDT setup during loading.

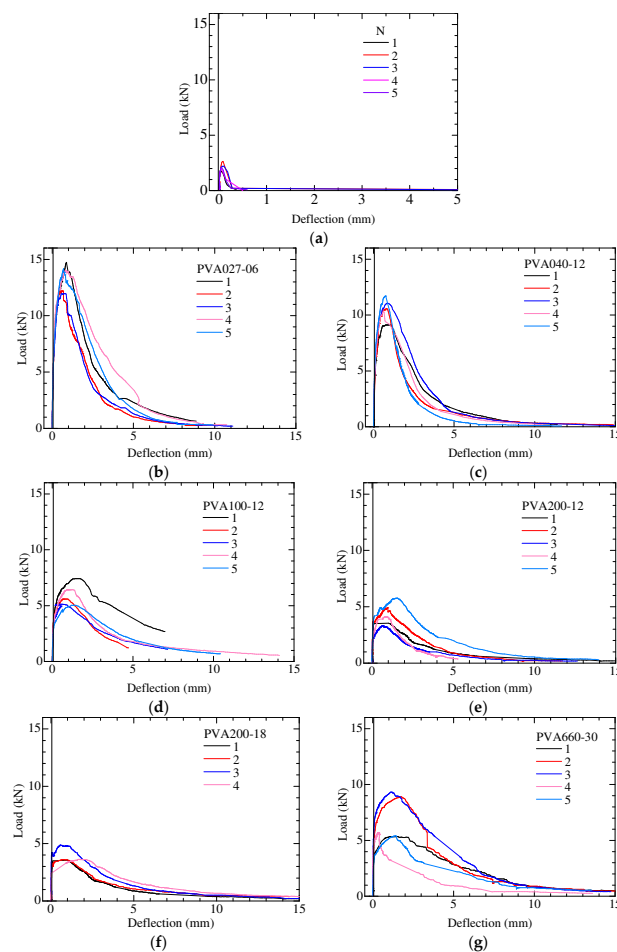


Figure 6. Load–deflection (LPD) relationship of PVA-FRCC: (a) N; (b) PVA027-06; (c) PVA040-12; (d) PVA100-12; (e) PVA200-12; (f) PVA200-18; (g) PVA660-30.

The specimen without fiber shows very low loading capacity and a small deflection before failure. The loading capacity increases by adding fiber, but it is observed that the loading capacity decreases as the diameter of the fiber increases. From specimens PVA 200-12 and PVA 200-18, it can be observed that the load capacity of PVA-FRCC is little affected by the fiber length. The summary of the test results is shown in Table 4. CMOD is calculated from the measured deformation by the two Pi-type displacement transducers, assuming that the plain section remains plain. Figure 7 shows the average maximum load and the fracture energy, and the error bar indicates the range of the values. The fracture energy is calculated using Equation (1).

$$G_F = \frac{W}{A_{lig}} \quad (1)$$

where, G_F = fracture energy (N/mm), W = area below load–LPD curve up to 15 mm (N·mm), and A_{lig} = area of the ligament (mm²).

Table 4. Three-point bending test result.

Specimen ID	Avg. Max. Load (kN)	Avg. Max. Moment (kN·m)	Avg. CMOD at Max. Load (mm)	Avg. Fracture Energy (N/mm)
N	2.13	0.160	0.056	0.07
PVA027-06	13.43	1.007	1.004	3.70
PVA040-12	10.56	0.792	1.039	2.77
PVA100-12	5.93	0.444	1.881	2.48
PVA200-12	4.40	0.330	1.368	1.53
PVA200-18	4.35	0.326	1.457	1.74
PVA660-30	6.94	0.521	2.200	3.38

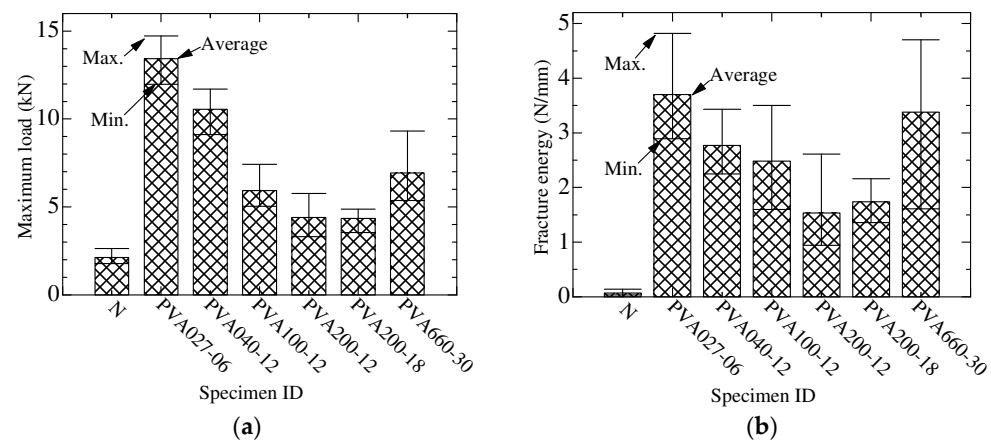


Figure 7. Three-point bending test result: (a) Maximum load; (b) Fracture energy.

3. Adaptability of Bridging Law Calculation for PVA100-12

3.1. Single-Fiber Pullout Model and Calculation of Bridging Law

The bridging law (tensile stress–crack width relationship) is calculated by summing the pullout loads of every bridging fiber, in which the single-fiber pullout behavior is expressed by a tri-linear model for PVA fiber [39]. Figure 8 shows the proposed tri-linear model for PVA100-12 fiber that has values of the first peak load, P_a , and the maximum, P_{max} , are equal to 1.5 N and 3.0 N, and the values of crack width at the first peak load, w_a , and the maximum, w_{max} , are 0.2 mm and 0.45 mm, respectively. The pullout load becomes zero when the crack width equals the embedded length, l_b , on the shorter side of a single fiber [39]. Ozu et al. studied the adaptability of the proposed bridging model using the results of a three-point bending test with notched specimens and section analysis. The test

result and the analysis value show good agreement when the orientation intensity, k , is 0.4 [42]. The same value for orientation intensity is also adopted in this study.

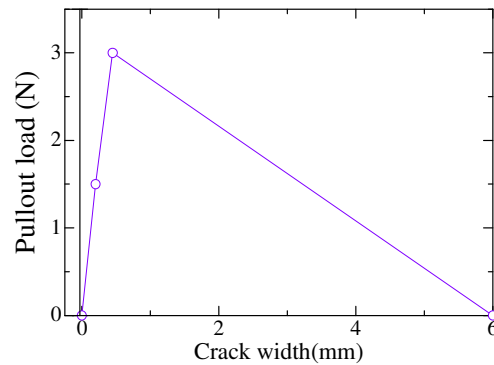


Figure 8. Tri-linear model for single-fiber pullout load–crack width relationship for PVA100-12.

The result of the bridging law calculation is shown in Figure 9. As shown in the left figure, the tensile stress–crack width relationship shows the sudden fiber rupture of some of the fibers after the peak, and the final stage shows a gradual slip out of the fibers. This phenomenon is also shown in the fiber-effectiveness crack width relationship shown in the right figure. This relationship shows the ratio of the number of effective bridging fibers that are not pulled out or ruptured and supporting bridging forces to the theoretical number of fibers within a target volume.

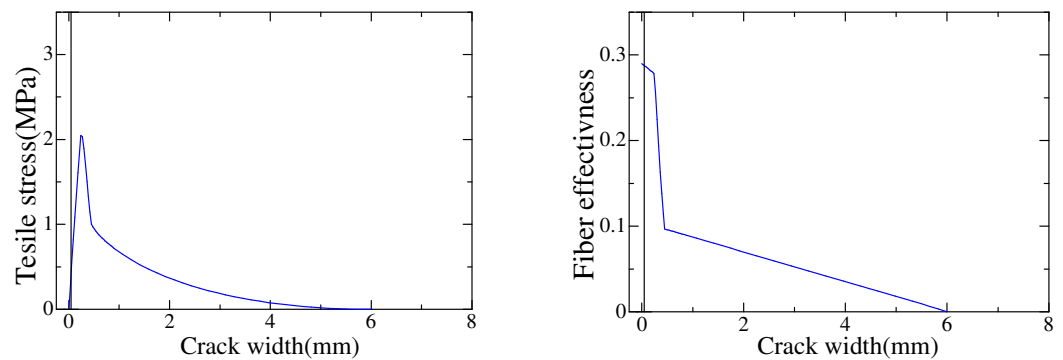


Figure 9. Bridging law calculation results of PVA100-12.

3.2. Section Analysis

The section analysis is conducted to evaluate the bending strength and checks the model’s adaptability to the experimental result. The analysis is carried out based on the assumption that plain section remains plain considering the compatibility condition of deformation and rotation angle, as same as those by Ozu et al. [42]. The equivalent compressive length, $l_{c,eq}$, is calculated by fitting the initial slope of the section analysis results to the measured load-CMOD curves in the bending test. For the tension side, the Popovics model is adopted for the tensile stress–crack width relationship to obtain a better fit with the bridging law calculation, as shown in Equation (2).

$$\frac{\sigma}{\sigma_{max}} = \frac{w}{w_{max}} \cdot \frac{n}{(n - 1) \cdot (w/w_{max})^n} \tag{2}$$

where, σ_{max} is the maximum tensile stress from the bridging law calculation; w_{max} is the crack width at maximum tensile stress; and n is Popovics constant, which is obtained by the fitting calculation of the bridging law calculation result.

Figure 10 compares the Popovics model and bridging law calculation for PVA100-12. The Popovics constant is 2.75.

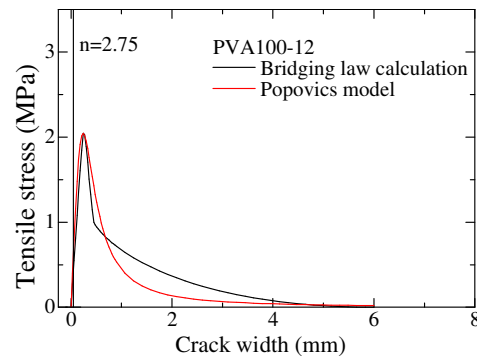


Figure 10. Comparison of Popovics model and bridging law calculation result of PVA100-12.

Figure 11 compares the bending moment–CMOD relationship between the analysis and the bending test of PVA100-12 specimens. As shown in the figure, the section analysis and the experimental result of the bending test of the notched specimens show good agreement in the maximum bending moment. The discrepancy between the analysis and test results at the post-peak is considered to be due to how actual cracks occur in the bending test. If multiple cracks occur or if the cracks do not progress straight toward the loading point, it is considered that the deformation has become larger.

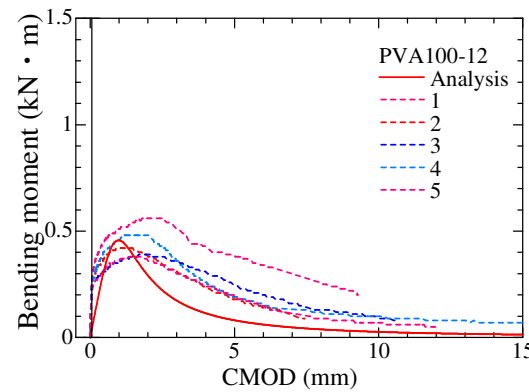


Figure 11. Comparison of bending moment–CMOD relationship for PVA100-12.

4. Bridging Law Considering the Influence of Fiber Dimensions

4.1. Single-Fiber Pullout Model and Calculation of Bridging Law

Since the proposed single-fiber pullout model by Kanakubo et al. shows a good agreement with the experimental result in the maximum bending moment as discussed in Section 3, the single-fiber pullout models for different fiber dimensions are developed based on the properties of the single-fiber pullout model for PVA100-12 fiber.

The first peak load, P_a , results from the debonding of the chemical bond between PVA and the matrix [36,37]. The fibers used for the study are the same fiber types with different dimensions, so they have the same chemical composition. Therefore, the first peak load is assumed to have proportional relations with the fiber perimeter. By considering the perimeter of PVA100-12, $\phi_{f,100}$, and its first peak load value, $P_{a,100}$, a relationship shown in Equation (3) is developed.

$$P_a = \frac{P_{a,100} \times \phi_f}{\phi_{f,100}} = \frac{1.5 \times \pi \times d_f}{\pi \times 100} = 0.015d_f \tag{3}$$

where, P_a is the first peak load (N), ϕ_f is the perimeter (μm), and d_f is the diameter (μm) of the fiber under consideration.

The debonding of the chemical bond is assumed to cause the same slip from the matrix regardless of the fiber dimension, so the same crack width with PVA100-12 fiber at first peak load, w_a , is considered for all fiber dimensions ($w_a = 0.2 \text{ mm}$).

The maximum pullout load, P_{max} , is determined using the fundamental bond equilibrium conditions that Asano et al. developed based on the relationship between the bond strength and bond fracture energy [43]. This relationship was originally developed for reinforced concrete members by the theoretical bond problem, and the bond strength is solved by integrating the bond stress distribution. The basic differential equation of the bond problem is shown in Equation (4) [44].

$$\frac{d^2s}{dx^2} = \frac{1 + n\rho}{E_f \cdot A_f} \phi_f \tau_f \quad (4)$$

where, s is the slip of the fiber, ϕ_f , A_f , and E_f are the perimeter, cross-sectional area, and elastic modulus of the fiber, τ_f is the bond stress, n is the ratio of elastic modulus of the fiber to the matrix, and ρ is the ratio of the cross-sectional area of the fiber to the matrix.

By solving Equation (4) under arbitrary boundary conditions, the value of slip of the fiber can be determined, as shown in following Equations.

$$\text{Let } v_f = \frac{1 + n\rho}{E_f \cdot A_f} \phi_f \quad (5)$$

$$\therefore \frac{d^2s}{dx^2} = v_f \tau_f \quad (6)$$

$$\therefore 2 \frac{ds}{dx} \frac{d^2s}{dx^2} = 2 v_f \frac{ds}{dx} \tau_f \quad (7)$$

$$\therefore \frac{d}{dx} \left(\frac{ds}{dx} \right)^2 = 2 v_f \frac{ds}{dx} \tau_f \quad (8)$$

$$\therefore \left(\frac{ds}{dx} \right)^2 = 2 v_f \int \tau_f ds + C_1 \quad (9)$$

$$\therefore \frac{ds}{dx} = \sqrt{2 v_f \int \tau_f ds + C_1} \quad (10)$$

In the case of a pullout load with sufficiently enough embedded length, the tensile force becomes 0 when the slip is 0, so the constant $C_1 = 0$.

On the other hand, integrating both sides of Equation (4) gives the following:

$$\frac{ds}{dx} = \frac{1 + n\rho}{E_f \cdot A_f} \cdot \phi_f \int \tau_f dx = \frac{1 + n\rho}{E_f \cdot A_f} \cdot P = \frac{v_f}{\phi_f} \cdot P \quad (11)$$

where, P is pullout load of fiber. Equations (10) and (11) give Equation (12).

$$\frac{v_f}{\phi_f} \cdot P = \sqrt{2 v_f \int \tau_f ds} \quad (12)$$

If the embedded length is sufficiently large, then the maximum tensile force, P_{max} , is given by Equation (13).

$$\frac{v_f}{\phi_f} \cdot P_{max} = \sqrt{2 v_f \int_0^\infty \tau_f ds} \quad (13)$$

While, bond fracture energy, G_{fb} , is given by the following:

$$G_{fb} = \int_0^{s_u} \tau_f ds \quad (14)$$

And considering that τ_f becomes 0 when the slip exceeds slip at ultimate, s_u , Equation (15) can be derived.

$$\frac{v_f}{\phi_f} \cdot P_{max} = \sqrt{2 v_f \cdot G_{fb}} \quad (15)$$

Rearranging Equation (15) gives the following:

$$P_{max} = \sqrt{\frac{2 G_{fb} \cdot \phi_f^2}{\nu_f}} = \sqrt{\frac{2 G_{fb} \cdot E_f \cdot A_f \cdot \phi_f}{1 + n\rho}} \tag{16}$$

If the stiffness of the matrix is sufficiently large, the deformation of the matrix can be ignored, then ($n\rho \rightarrow 0$).

$$\therefore P_{max} = \sqrt{2 G_{fb} \cdot E_f \cdot A_f \cdot \phi_f} \tag{17}$$

where, G_{fb} is bond fracture energy (N/mm), E_f , A_f , and ϕ_f are the elastic modulus (MPa), cross-sectional area (mm²), and perimeter (mm) of the fiber under consideration, respectively.

The fibers used have the same chemical composition with different dimensions, so the bond fracture energy is calculated from the already-known value of the maximum pullout load of PVA100-12 fiber. In addition, when the same chemical composition of PVA fibers is assumed to have the same bond fracture energy and elastic modulus, Equation (17) can give the proportional relationships with d_f powered by 3/2, as shown in Equation (18).

$$P_{max} \propto \sqrt{d_f^3} \tag{18}$$

To determine the slip of the fiber at the loaded end (crack surface), solving Equation (4) is necessary. However, the limited functions of τ_f , such as constant or proportional relation of the slip, can only mathematically solve Equation (4). When the constant τ_f which has the same bond fracture energy is assumed, the maximum tensile force, P_{max} , is given by Equation (19).

$$P_{max} = \tau_f \cdot \phi_f \cdot s_{max} \propto d_f \cdot s_{max} \tag{19}$$

where, s_{max} is the slip of the fiber at the maximum tensile force. Comparing Equations (18) and (19), it can be assumed that s_{max} has a proportional relationship with $\sqrt{d_f}$. The crack width at maximum load, w_{max} , can be determined from s_{max} . Considering the pullout model value for the crack width at maximum load, w_{max} , of PVA100-12, a constant of proportionality is determined for the equation.

$$w_{max} = w_{max,100} \sqrt{\frac{d_f}{d_{f,100}}} = 0.045 \sqrt{d_f} \tag{20}$$

where, w_{max} is the crack width at maximum pullout load (mm) and d_f is the diameter (μm) of the fiber under consideration.

The pullout load becomes zero when the crack width equals the embedded length of the short side of the fiber, l_b .

Figure 12 shows the developed single-fiber pullout model for the PVA fibers with different dimensions. The model for PVA100-12 is the same one shown in Figure 8. Figure 12 shows the models when the embedded length is equal to half of the fiber length. When the embedded length becomes smaller than half of the fiber length, the decline after the peak becomes steep.

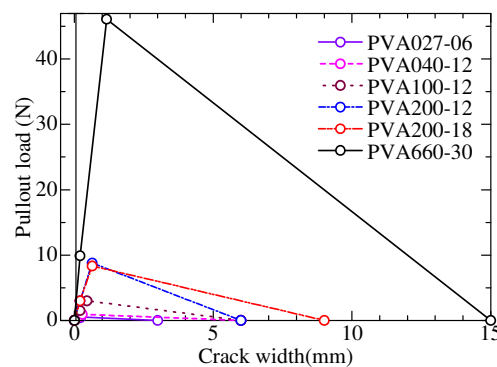


Figure 12. Single-fiber pullout model for different fiber dimensions.

Based on the developed tri-linear single-fiber pullout model for the different fiber dimensions above, a bridging law calculation is used to study the influence of fiber dimensions on the bridging performance of PVA-FRCC. The parameters for the bridging law calculation are listed in Table 5. The calculated values for the single-fiber pullout model are also shown in this table. The nominal strengths provided by the manufacturer are multiplied by 0.645 to express the fiber strength in the matrix, as in the case of PVA100-12 (774 MPa = 1200 MPa × 0.645).

Table 5. Parameters of bridging law calculation for different fiber dimensions.

Parameter	PVA027-06	PVA040-12	PVA100-12	PVA200-12	PVA200-18	PVA660-30
First peak load, P_a (N)	0.4	0.6	1.5	3.0	3.0	9.9
Crack width at P_a , w_a (mm)	0.2	0.2	0.2	0.2	0.2	0.2
Maximum load, P_{max} (N)	0.5	0.9	3.0	8.8	8.3	46.1
Crack width at P_{max} , w_{max} (mm)	0.23	0.28	0.45	0.64	0.64	1.16
Fiber strength, σ_{fi} (MPa)	1161	1006	774	587	629	581

Snubbing coefficient, $f = 0.5$; Fiber strength reduction factor, $f' = 0.3$; Fiber orientation intensity, $k = 0.4$; Fiber volume fraction, $V_f = 2\%$; Bond fracture energy, $G_{fb} = 0.0651$ N/mm.

The result of the bridging law calculation is shown in Figure 13. The left figure shows the tensile stress–crack width relationship. The calculation result for PVA 100-12 is the same as in Figure 9. The tensile stress decreases as the fiber diameter increases, but most of the smaller-diameter fibers rupture, which is described by a sudden drop in the curve after the maximum tensile stress. Whereas, when the diameter of the fiber increases, the rupturing of the fibers decreases and shows a behavior of pulling out of the matrix, which is described by a gentle slope of softening curves. The result of PVA600-30 shows that the maximum tensile stress and the inflection tensile stress are equal, which implies that there is no ruptured fiber. This phenomenon is also shown in the fiber effectiveness curve. At zero crack width, all the fibers have the same fiber effectiveness since the same fiber orientation intensity is used.

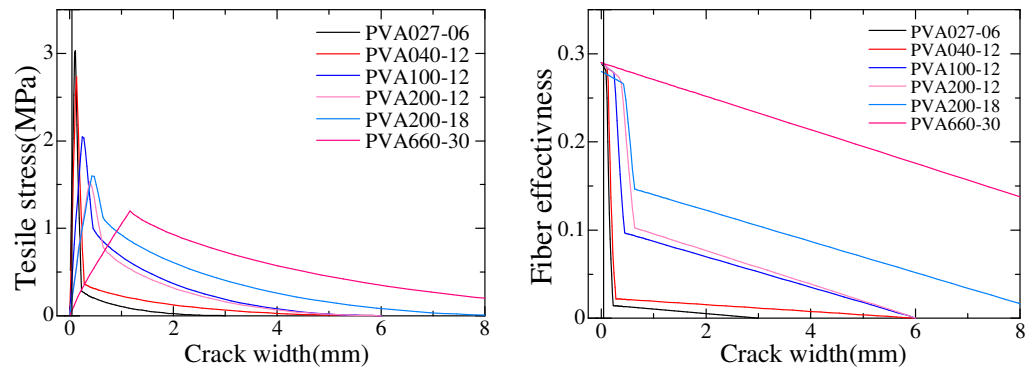


Figure 13. Bridging law calculation results.

4.2. Section Analysis and Its Adaptability

The section analysis based on the calculated bridging law is conducted to evaluate the bending strength. The section analysis for the different fiber dimensions is carried out using the same assumption and calculation method as in Section 3.2. Figure 14 shows the fitting curve of the Popovics model to the bridging law calculation. The value of Popovics constant, n , is shown at the left top of the graph for each specimen. The model for PVA100-12 is the same as shown in Figure 10.

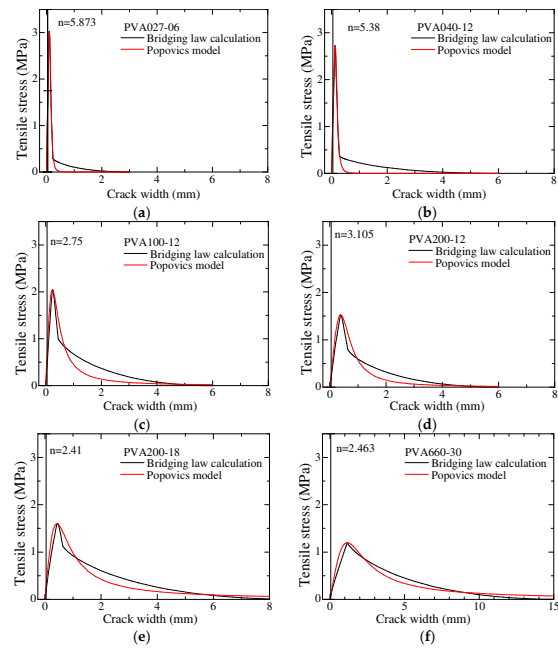


Figure 14. Comparison of Popovics model and bridging law calculation of PVA-FRCC: (a) PVA027-06; (b) PVA040-12; (c) PVA100-12; (d) PVA200-12; (e) PVA200-18; and (f) PVA660-30.

Figure 15 compares the bending moment–CMOD relationship between the analysis and the bending test results. The curves for PVA100-12 are the same ones shown in Figure 11. For the smaller fibers, CMOD at the peak load and the softening branch in the test results show larger values than the analysis. These differences are considered because of the fine cracks generated when bending specimens. The section analysis conducted in this study considers only one crack opening. For the larger-diameter fibers, stiffer slopes before the peaks are observed in the test results. This is due to the bridging law adaptation for section analysis, where the elastic part of the matrix before cracking is ignored. The softening branch in the test results shows good agreement with the analysis results.

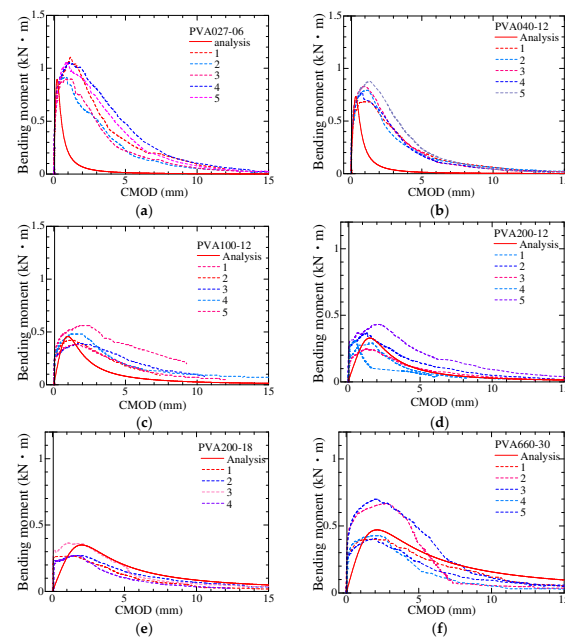


Figure 15. Bending moment–CMOD relationship of PVA-FRCC: (a) PVA027-06; (b) PVA040-12; (c) PVA100-12; (d) PVA200-12; (e) PVA200-18; (f) PVA660-30.

Table 6 lists the results of the maximum moment of the section analysis and the test. It can be seen from the results that the maximum bending moment of PVA027-06 is much greater than the other fiber dimensions. The maximum moment decreases as the dimension of the fiber increases in both cases. The ratio of the maximum moment of the test to analysis is around 1.0, and the maximum deviation is 13%, which shows good agreement between the test and the analysis results.

Table 6. Comparison of maximum moment between bending test and analysis.

ID	Maximum Moment (kN·m)		Ratio of Maximum Moment of the Test to the Analysis Result
	Test	Analysis	
PVA027-06	1.007	0.895	1.13
PVA040-12	0.792	0.773	1.02
PVA100-12	0.444	0.457	0.97
PVA200-12	0.330	0.329	1.00
PVA200-18	0.326	0.350	0.93
PVA660-30	0.521	0.470	1.11

5. Conclusions

To investigate the influence of fiber dimensions on the bridging performance of PVA-FRCC, a bending test, bridging law calculation, and section analysis were conducted. The main parameters of this study are the diameter and length of PVA fiber. The following conclusions are made based on the results obtained from this study:

1. From the bending test, it was found that the load capacity of PVA-FRCC with 27 μm diameter fiber (PVA027-06) is much higher than the other specimens, and the load capacity decreases as the fiber diameter increases.
2. From the bending test, bridging law calculation, and section analysis results of different fiber lengths of FRCC with the same diameter (PVA200-18 and PVA200-12), the length of the fiber has a small effect on the load capacity and the bridging performance of PVA-FRCC.
3. The parameters that give the characteristic points of the tri-linear model for the single-fiber pullout model are proposed as functions of diameter, bond fracture energy, elastic modulus, cross-sectional area, and fiber perimeter.
4. According to the bridging law calculation, the maximum bridging stress decreases as the fiber diameter increases. Most of the fibers with smaller diameters ruptured after the peak, while most of the fibers with bigger diameters slipped out of the matrix.
5. Section analysis is conducted to verify the proposed model. The ratio of the maximum bending moment of the experiment to the analysis ranged from 0.93 to 1.13, which can lead to the conclusion that the proposed model shows a good agreement with the experiment result.

6. Recommendation

In this study, the adaptability of the developed single-fiber pullout model is checked through a bending test using only six fiber dimensions. However, to strengthen the model, it is necessary to carry out more investigation using more fiber dimensions and test methods. After extensive research, a relationship between bridging stress and fiber dimension can be developed.

Supplementary Materials: The following supporting information can be downloaded at: <https://www.mdpi.com/article/10.3390/fib12080070/s1>.

Author Contributions: Conceptualization, H.N.S., S.F.A. and T.K.; methodology, H.N.S. and T.K.; validation, H.N.S. and T.K.; formal analysis, H.N.S.; investigation, H.N.S., S.F.A. and T.K.; data curation, H.N.S.; writing—original draft preparation, H.N.S.; writing—review and editing, T.K., M.V.R.S. and S.B.S.; visualization, H.N.S., S.F.A. and T.K.; supervision, T.K., M.V.R.S. and S.B.S.; project administration, T.K. and S.B.S. All authors have read and agreed to the published version of the manuscript.

Funding: This research was funded by the Japan Society for the Promotion of Science, India–Japan Cooperative Science Program (DST) Grant Number 120237702.

Data Availability Statement: The original contributions presented in the study are included in the Supplementary Materials. Further inquiries can be directed to the corresponding author.

Conflicts of Interest: The authors declare no conflicts of interest.

Nomenclature

A_f	Cross-sectional area of fiber (mm ²)
A_{lig}	Area of the ligament (mm ²)
d_f	Diameter of fiber (μm)
$d_{f,100}$	Diameter of fiber for PVA 100-12 (μm)
E_f	Elastic modulus of fiber (MPa)
f	Snubbing coefficient
f'	Fiber strength reduction factor
G_F	Fracture energy (N/mm)
G_{fb}	Bond fracture energy (N/mm)
k	Fiber orientation intensity
l_b	Embedded length of a single fiber (mm)
$l_{c,eq}$	Equivalent compressive length (mm)
n	Popovics constant, ratio of elastic modulus of fiber to matrix
P_a	First peak load (N)
$P_{a,100}$	First peak load for PVA100-12 (N)
P_{max}	Maximum pullout/tensile load (N)
s	Slip of fiber (mm)
s_{max}	Slip of fiber at the maximum tensile force (mm)
s_u	Slip of fiber at ultimate (mm)
V_f	Fiber volume fraction (%)
W	Area below load–LPD curve (N·mm)
w_a	Crack width at the first peak load (mm)
w_{max}	Crack width at the maximum load (mm)
ϕ_f	Perimeter of fiber (μm)
$\phi_{f,100}$	Perimeter of PVA100-12 fiber (μm)
ρ	Ratio of the cross-sectional area of the fiber to the matrix
σ	Tensile stress (MPa)
σ_{fu}	Fiber strength (MPa)
σ_{max}	Maximum tensile stress (MPa)
τ_f	Bond stress (MPa)

References

- Chandrathilaka, E.R.K.; Baduge, S.K.; Mendis, P.; Thilakarathna, P.S.M. Structural applications of synthetic fiber reinforced cementitious composites: A review on material properties, fire behavior, durability, and structural performance. *Structures* **2021**, *34*, 550–574. [\[CrossRef\]](#)
- Shah, S.P.; Rangan, B.V. Fiber Reinforced Concrete Properties. *J. Proc.* **1971**, *68*, 126–137. [\[CrossRef\]](#)
- Tošić, N.; Aidarov, S.; de la Fuente, A. Systematic Review on the Creep of Fiber-Reinforced Concrete. *Materials* **2020**, *13*, 5098. [\[CrossRef\]](#) [\[PubMed\]](#)
- Ahmed, S.F.U.; Mihashi, H. A review on durability properties of strain hardening fiber reinforced cementitious composites (SHFRCC). *Cem. Concr. Compos.* **2007**, *29*, 365–376. [\[CrossRef\]](#)
- Aydın, S. Effects of fiber strength on fracture characteristics of normal and high strength concrete. *Per. Pol. Civ. Eng.* **2013**, *57*, 191. [\[CrossRef\]](#)
- Naik, T.R. Sustainability of Concrete Construction. *Pract. Period Struct. Des. Constr.* **2008**, *13*, 98–103. [\[CrossRef\]](#)
- Kasagani, H.; Rao, C.B.K. Effect of graded fibers on stress-strain behavior of Glass Fiber Reinforced Concrete in tension. *Constr. Build. Mater.* **2018**, *183*, 592–604. [\[CrossRef\]](#)
- Parameswaran, V.S. Fibre-reinforced concrete: A versatile construction material. *Build. Environ.* **1991**, *26*, 301–305. [\[CrossRef\]](#)
- Li, V.C. Large volume, high-performance applications of fibers in civil engineering. *J. Appl. Polym. Sci.* **2002**, *83*, 660–686. [\[CrossRef\]](#)

10. Labib, W.A. Fibre Reinforced Cement Composites. In *Cement Based Materials*; Saleh, H.E.-D.M., Rahman, R.O.A., Eds.; InTech: London, UK, 2018. [CrossRef]
11. Mu, Y.; Yasojima, A.; Kanakubo, T. Shear Performance of FRCC Beam-Column Joints Using Various Polymer Fibers. *J. Civ. Eng. Archit.* **2019**, *13*, 562–571. [CrossRef]
12. Bentur, A.; Mindess, S. *Fibre Reinforced Cementitious Composites*, 2nd ed.; Taylor & Francis: London, UK, 2007.
13. Kanakubo, T. Tensile Characteristics Evaluation Method for Ductile Fiber-Reinforced Cementitious Composite. *J. Adv. Concr. Technol.* **2006**, *4*, 3–17. [CrossRef]
14. Sagar, B.; Sivakumar, M.V.N. Compressive properties and analytical modeling for stress-strain curves of polyvinyl alcohol fiber reinforced concrete. *Constr. Build. Mater.* **2021**, *291*, 123192. [CrossRef]
15. Atahan, H.N.; Pekmezci, B.Y.; Tuncel, E.Y. The behavior of PVA Fiber-Reinforced Cementitious Composites under Static and Impact Flexural Effects. *J. Mater. Civ. Eng.* **2013**, *25*, 1438–1445. [CrossRef]
16. Naaman, A.E.; Reinhardt, H.W. *High-Performance Fiber Reinforced Cement Composites 2: Proceedings of the International Workshop*; CRC Press: London, UK, 2004.
17. Pan, Y. Mechanical and Microstructural Characteristics of the Fiber-Reinforced Composite Materials. *J. Miner. Mater. Charact. Eng.* **2022**, *10*, 477–488. [CrossRef]
18. Pakravan, H.R.; Ozbakkaloglu, T. Synthetic fibers for cementitious composites: A critical and in-depth review of recent advances. *Constr. Build. Mater.* **2019**, *207*, 491–518. [CrossRef]
19. Ding, Y.; Yu, K.; Li, M. A review on high-strength engineered cementitious composites (HS-ECC): Design, mechanical property and structural application. *Structures* **2022**, *35*, 903–921. [CrossRef]
20. Lan, M.; Zhou, J.; Xu, M. Effect of Fibre Types on the Tensile Behaviour of Engineered Cementitious Composites. *Front. Mater.* **2021**, *8*, 775188. [CrossRef]
21. Meng, D.; Huang, T.; Zhang, Y.X.; Lee, C.K. Mechanical behavior of a polyvinyl alcohol fiber reinforced engineered cementitious composite (PVA-ECC) using local ingredients. *Constr. Build. Mater.* **2017**, *141*, 259–270. [CrossRef]
22. Huang, T.; Zhang, Y.X. Mechanical Properties of a PVA Fiber Reinforced Engineered Cementitious Composite. *Proc. Int. Struct. Eng. Constr.* **2014**, *1*, 439–444. [CrossRef]
23. Li, V.C. From Micromechanics to Structural Engineering: The Design of Cementitious Composites for Civil Engineering Applications. *Doboku Gakkai Ronbunshu* **1993**, *1993*, 1–12. [CrossRef]
24. Kim, D.J.; Naaman, A.E.; El-Tawil, S. Comparative flexural behavior of four fiber reinforced cementitious composites. *Cem. Concr. Compos.* **2008**, *30*, 917–928. [CrossRef]
25. Fakharifar, M.; Dalvand, A.; Arezoumandi, M.; Sharbatdar, M.K.; Chen, G.; Kheyroddin, A. Mechanical properties of high-performance fiber reinforced cementitious composites. *Constr. Build. Mater.* **2014**, *71*, 510–520. [CrossRef]
26. Zhang, J.; Wang, Z.; Wang, Q.; Gao, Y. Simulation and test of the flexural performance of polyvinyl alcohol-steel hybrid fiber reinforced cementitious composite. *J. Compos. Mater.* **2016**, *50*, 4291–4305. [CrossRef]
27. Plagué, T.; Desmettre, C.; Charron, J.P. Influence of fiber type and fiber orientation on cracking and permeability of reinforced concrete under tensile loading. *Cem. Concr. Res.* **2017**, *94*, 59–70. [CrossRef]
28. Kanakubo, T.; Koba, T.; Yamada, K. Flexural Characteristics of Functionally Graded Fiber-Reinforced Cementitious Composite with Polyvinyl Alcohol Fiber. *J. Compos. Sci.* **2021**, *5*, 94. [CrossRef]
29. Kanda, T.; Li, V.C. Effect of Fiber Strength and Fiber-Matrix Interface on Crack Bridging in Cement Composites. *J. Eng. Mech.* **1999**, *125*, 290–299. [CrossRef]
30. Kanda, T.; Li, V.C. Interface Property and Apparent Strength of High-Strength Hydrophilic Fiber in Cement Matrix. *J. Mater. Civ. Eng. ASCE* **1998**, *10*, 5–13. [CrossRef]
31. Suthiwarapirak, P.; Matsumoto, T.; Kanda, T. Multiple Cracking and Fiber Bridging Characteristics of Engineered Cementitious Composites under Fatigue Flexure. *J. Mater. Civ. Eng.* **2004**, *16*, 433–443. [CrossRef]
32. Yang, E.H.; Wang, S.; Yang, Y.; Li, V.C. Fiber-Bridging Constitutive Law of Engineered Cementitious Composites. *J. Adv. Concr. Technol.* **2008**, *6*, 181–193. [CrossRef]
33. Lin, C.; Kayali, O.; Morozov, E.V.; Sharp, D.J. Influence of fiber type on flexural behavior of self-compacting fiber reinforced cementitious composites. *Cem. Concr. Compos.* **2014**, *51*, 27–37. [CrossRef]
34. Ling, Y.; Zhang, P.; Wang, J.; Chen, Y. Effect of PVA fiber on mechanical properties of cementitious composite with and without nano-SiO₂. *Constr. Build. Mater.* **2019**, *229*, 117068. [CrossRef]
35. Zhang, P.; Ling, Y.; Wang, J.; Shi, Y. Bending Resistance of PVA Fiber Reinforced Cementitious Composites Containing Nano-SiO₂. Available online: <https://www.degruyter.com/document/doi/10.1515/ntrev-2019-0060/html> (accessed on 30 July 2024).
36. Wang, S.; Li, V.C. Polyvinyl Alcohol Fiber Reinforced Engineered Cementitious Composites: Material Design and Performances. In *Proceedings of the International Workshop on High Performance Fiber Reinforced Cementitious Composites (HPFRCC) in Structural Applications*, Honolulu HI, USA, 23–26 May 2005.
37. Li, V.C.; Wang, S.; Wu, C. Tensile strain-hardening behavior of polyvinyl alcohol engineered cementitious composite (PVA-ECC). *ACI Mater. J.* **2001**, *98*, 483–492.
38. Wang, H.L.; Peng, G.Y.; Luo, Y.J.; Sun, X.Y. Uniaxial Tensile Experiment on PVA Fiber Reinforced Cementitious Composites. *Appl. Mech. Mater.* **2013**, 438–439. [CrossRef]

39. Kanakubo, T.; Miyaguchi, M.; Asano, K. Influence of Fiber Orientation on Bridging Performance of Polyvinyl Alcohol Fiber-Reinforced Cementitious Composite. *ACI Mater. J.* **2016**, *113*, 131. [[CrossRef](#)]
40. *JIS A 6201*; Fly Ash for Use in Concrete. Japanese Standards Association (JSA): Tokyo, Japan, 2015.
41. *ISO 19044*; Test Methods for Fiber-Reinforced Cementitious Composites-Load Displacement Curve Using a Notched Specimen. ISO: Geneva, Switzerland, 2016.
42. Ozu, Y.; Miyaguchi, M.; Kanakubo, T. Modeling of Bridging Law for PVA Fiber-Reinforced Cementitious Composite Considering Fiber Orientation. *J. Civ. Eng. Archit.* **2018**, *12*, 651–661. [[CrossRef](#)]
43. Asano, K.; Yasojima, A.; Kanakubo, T. Study on bond splitting behavior of reinforced concrete members. Part 6 Theoretical solution by the parabolic model of bond constitutive law. *J. Struct. Constr. Eng. AIJ* **2008**, *73*, 641–646. (In Japanese) [[CrossRef](#)]
44. Rehm, G. *Über die Grundlagen des Verbundes zwischen Stahl und Beton*. Deutscher Ausschuss für Stahlbeton; Schriftenreihe, Heft. 138; Ernst: Berlin, Germany, 1961.

Disclaimer/Publisher’s Note: The statements, opinions and data contained in all publications are solely those of the individual author(s) and contributor(s) and not of MDPI and/or the editor(s). MDPI and/or the editor(s) disclaim responsibility for any injury to people or property resulting from any ideas, methods, instructions or products referred to in the content.